Measurement of surface displacements with a UAV-borne/car-borne L-band DInSAR system: system performance and use cases

Othmar Frey
Gamma Remote Sensing /
Earth Observation & Remote Sensing,
ETH Zurich, Switzerland
Email: frey@gamma-rs.ch / otfrey@ethz.ch

Charles L. Werner
Andrea Manconi
Gamma Remote Sensing
Switzerland
Email: cw@gamma-rs.ch

Roberto Coscione
Earth Observation & Remote Sensing,
ETH Zurich, Switzerland

Abstract—In this paper, we present examples of DInSAR-based measurement of surface displacements using a novel compact L-band SAR system that can be mounted on mobile mapping platforms such as a UAV or a car. The good DInSAR system performance is demonstrated and, particularly, we also show a use case in which a car-borne system setup is employed to map surface displacements of a fast-moving landslide and the surrounding area in Switzerland. Our results show that car-borne and UAV-borne interferometric displacement measurements at L-band are feasible with high quality over various natural terrain. This novel compact DInSAR system for agile platforms complements existing terrestrial, airborne, and space-borne radar interferometry systems in terms of its new combination of (1) radar wavelength (sensitivity to displacement/decorrelation properties), (2) spatial resolution, (3) (near-) terrestrial observation geometry, and (4) mobile mapping capability.

Index Terms—SAR interferometry, mobile mapping, car-borne SAR, UAV, airborne SAR, surface displacements, landslide, geohazard, monitoring, terrestrial radar interferometer, back-projection, GPU, CUDA, interferometry, L-band, INS, GNSS.

I. INTRODUCTION

In this paper, we present examples of DInSAR-based measurement of surface displacements using a novel compact L-band SAR system that can be mounted on mobile mapping platforms such as a UAV or a car. This novel compact DInSAR system for agile platforms complements existing terrestrial, airborne, and space-borne radar interferometry systems in terms of its new combination of (a) radar wavelength (sensitivity to displacement/decorrelation properties), (b) spatial resolution, (c) (near-) terrestrial observation geometry, and (d) mobile mapping capability.

A number of groups have been working on UAV-borne or car-borne *SAR imaging* during the last decade [1]–[3]. We had presented first results on car-borne SAR imaging including a single-pass interferogram at Ku-band in [4] using a CUDA / GPU implementation [5] of a time-domain back-projection (TDBP) approach [6]–[8] that has been adapted to FMCW systems [3]–[5], [9] leading to focused complex SAR images directly in map coordinates. More recently, Palm et al. [10], [11] presented car-borne close-range high-resolution SAR imaging of radar backscatter of roads using a high-bandwidth FMCW system [12]. Over the last years, several authors have presented UAV-borne SAR systems and imaging using light-weight off-the-shelf quad- and octocopter UAVs [13]–[19] for different applications.
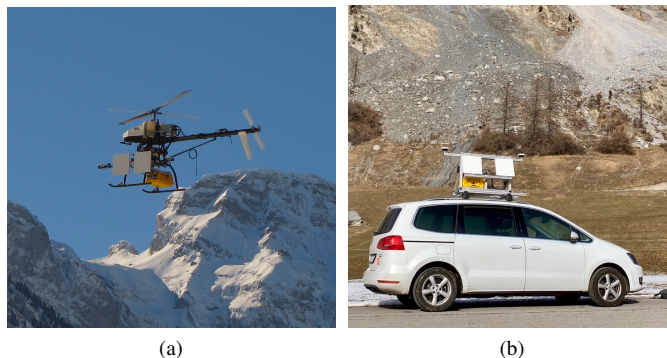

Fig. 1. (a) The compact FMCW L-band SAR system mounted on Aeroscout's UAV Scout B1-100 during an interferometric repeat-pass SAR data acquisition in Wolfenschiessen, Switzerland, in winter 2019. (b) Car-borne setup of the L-band SAR system in the landslide area in Brinzauls, in winter 2020. See also [20] for more details and system specifications of the SAR system.

Yet, area-wide mapping of surface displacements with repeat-pass SAR interferometry from custom moving platforms such as cars and low-flying UAVs has been a rather unexplored field so far.

In this paper, we demonstrate the DInSAR system performance of our recently developed modular L-band SAR system in combination with a TDBP-based data processing approach for high-resolution car-borne and UAV-borne mobile mapping of surface displacements—first results were presented in [20]. Particularly, we demonstrate mapping of surface displacements of a fast-moving landslide and surrounding area, in Brinzauls, Switzerland, a typical use case in which the car-borne system setup can be employed.

II. METHODS

Fig. 1 shows the UAV-borne (Scout B1-100 by Aeroscout GmbH) and car-borne configurations of the Gamma L-band SAR system with transmit and receive patch antennas, and the Honeywell HGuide n580 INS/GNSS navigation system. The L-band radar has 4 low-noise receiver channels that can operate simultaneously. The compact hardware with a total power consumption of less than 50W is aimed at UAV/airborne and car-borne mobile mapping or rail-based terrestrial operation. A detailed system specification table is available in Frey et al., 2019 [20]. While frequency-domain SAR focusing algorithms work well and efficiently for most spaceborne and
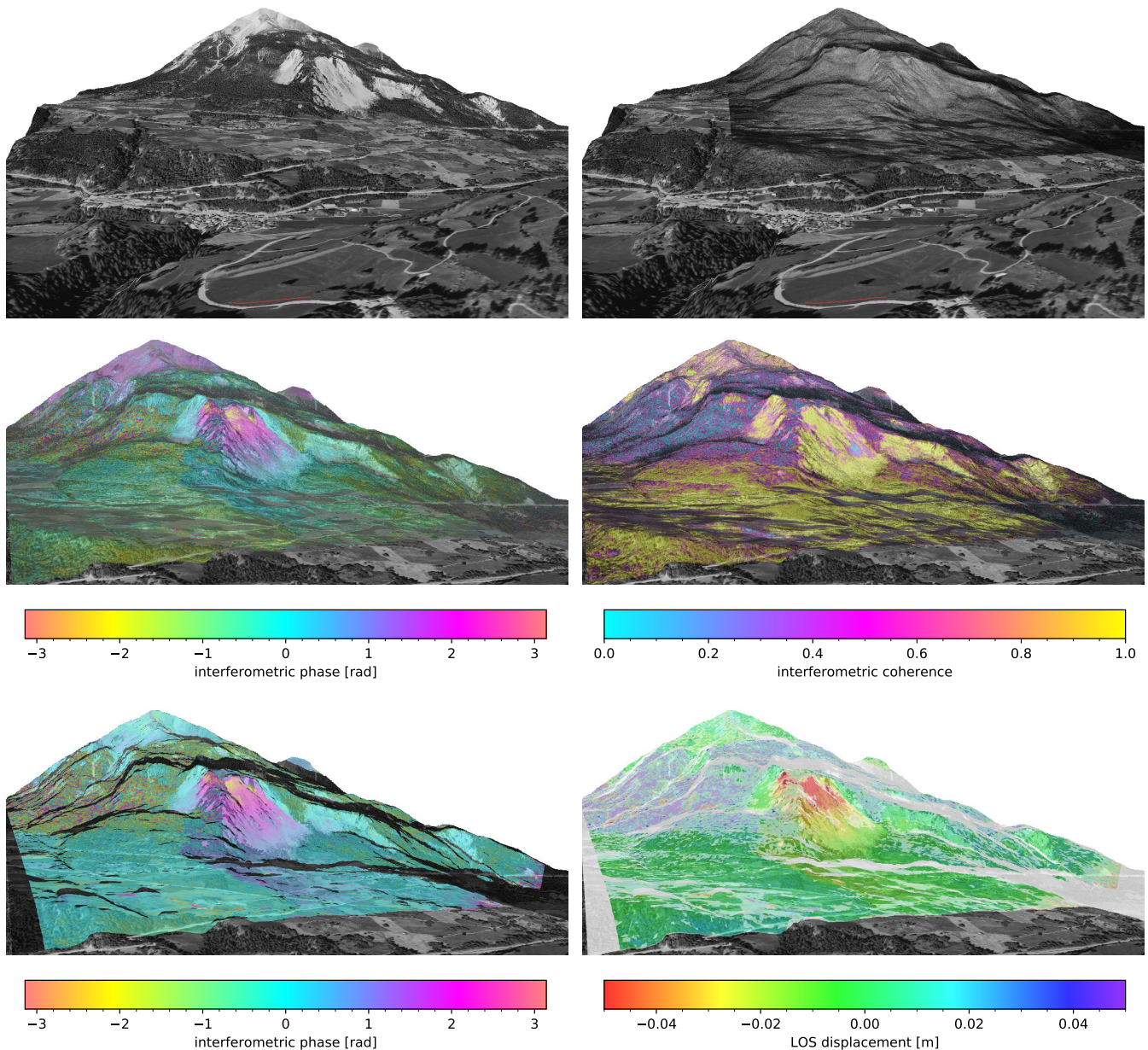
Fig. 2. Upper left: 3-D rendering of the test site with the landslide in Brinzauls, Switzerland. Orthophoto and digital elevation model ©swisstopo. The sensor trajectory of the car-borne reference L-band SAR data acquisition is shown as red curved line. Upper right: Overlay of reference SAR image (geoslc), focused directly to the 3-D topography represented by the DEM in map coordinates, and the orthophoto-rendered scene. Middle row: car-borne SAR 4-day unwrapped differential interferogram (left, rewrapped colorscale) and coherence (right)—each blended with a multi-look intensity image. Lower left: tropospheric-phase-corrected detrended 4-day unwrapped differential interferogram with shadow mask and view mask applied (rewrapped colorscale). Lower right: line-of-sight (LOS) displacement observed over 4 days (between 2020-01-20, 14:21and 2020-01-24, 11:25).

airborne acquisition scenarios they are less suited for more agile SAR platforms such as small UAVs or a car driving on a road. Therefore we apply a TDBP approach that can cope with arbitrarily shaped sensor trajectories. A time-domain back-projection (TDBP) approach [6], [7], which has been adapted to FMCW systems [3], [4], [9] and implemented for parallelized processing on GPUs [5], is employed to focus the car-borne or UAV-borne SAR data. Focusing directly to a DEM in map coordinates allows then to directly calculate the differential interferograms in map coordinates. Since highly-precise INS/GNSS systems were used for positioning and attitude determination of the SAR system the azimuth-varying baselines (due to the slightly different repeated tracks) are well-known and the topography induced phase can be removed by means of the TDBP-based focusing procedure and a high-resolution DEM (swissAlti3D, © swisstopo). The processing chain also includes a step to estimate and remove spatially low-frequent phase components that are attributed to spatiotemporal differences in tropospheric path delays and presence/absence of residual phase errors due to incorrect positioning can be tracked by subaperture processing (see also Fig. 3).
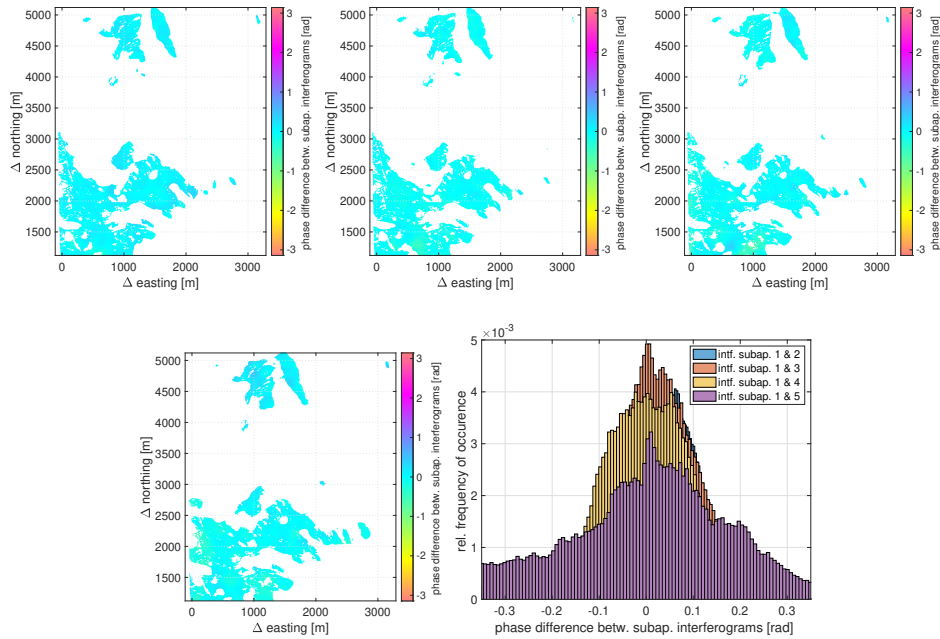
Fig. 3. Map of the differential phase of azimuth subaperture interferograms of the 4-day interferogram in Brinzauls indicating that no remaining large-scale phase trends are found between the 5 subapertures. The subplots show the phase maps between a) subaperture interferograms 1 & 2, b) 1 & 3, c) 1 & 4, d) 1 & 5, e) histogram of phase differences subaperture interferograms. Low-coherence areas were masked.

III. RESULTS AND DISCUSSION

A. Interferometric data products

In Fig. 2, the intermediate and final data products of the entire SAR imaging and interferometric processing chain are shown for a car-borne DInSAR data acquisition example at the site Brinzauls, Switzerland, where a fast-moving landslide poses a substantial hazard. The color scale is limited to ± 0.05m for visualization. LOS displacements of up to 0.08m m are found within the areas with a LOS displacement > 0.05m. The areas showing a coherence lower than the threshold of 0.7 are whitened (mostly forested areas seen at a very shallow view angles).

B. Precision of the measured displacement

To assess the precision of the interferometric phase measurement the formula by Rodriguez and Martin [21] can be used, which provides a means to estimate the interferometric phase standard deviation σ_ϕ (given that the number of looks $N_L \geq 4$) as a function of the interferometric coherence magnitude $|\gamma|$:

$$\sigma_\phi = \sqrt{\frac{1}{2 \cdot N_L} \frac{1 - |\gamma|^2)}{|\gamma|^2}} \qquad (1)$$

For a coherence threshold of $|\gamma| = 0.7$ and $N_L = 50$ looks the phase standard deviation $\sigma_\phi = 5.85^o (0.1 \text{ rad})$ which corresponds to a standard deviation of the line-of-sight displacement $\sigma_{dR} = 1.8$mm for this L-band SAR system. In the line-of-sight displacement map shown in Fig. 2 regions with a coherence below the threshold are masked (whitened).

C. Check for residual phase

The differential phase between various azimuth subaperture interferograms reveals residual phase trends/undulations [22] that are due to inaccurate acquisition geometry (typically induced by the limited accuracy of the INS/GNSS system and the modeling of the topography). To check for residual unwanted phase variations five subaperture images were processed per data set by TDBP-processing of five azimuth subsections. In Fig. 3 the differential phase maps and the phase histogram between those five azimuth subapertures are shown, which both indicate that no substantial remaining geometry-induced phase trends/undulations are present in the data.

D. Repeat-pass DInSAR performance in presence of vegetation

In Fig. 4 the interferometric phase and coherence maps for two cases of (1) near-zero spatial baseline and (2) approx. 3m spatial baseline are shown for the UAV-borne repeat-pass acquisitions. The short-term and almost zero-baseline interferogram shows excellent stable phase and coherence. With increasing baseline, the forested area shows, as expected, substantial volume decorrelation and phase changes due to uncompensated tree heights in the DEM. Keeping the repeat-pass spatial baseline as small as possible is essential, which can be challenging.

IV. CONCLUSION

We have demonstrated that DInSAR-based mobile mapping of surface displacement at L-band is feasible from agile platforms with high quality. The decorrelation properties at L-band in combination with the terrestrial observation geometries
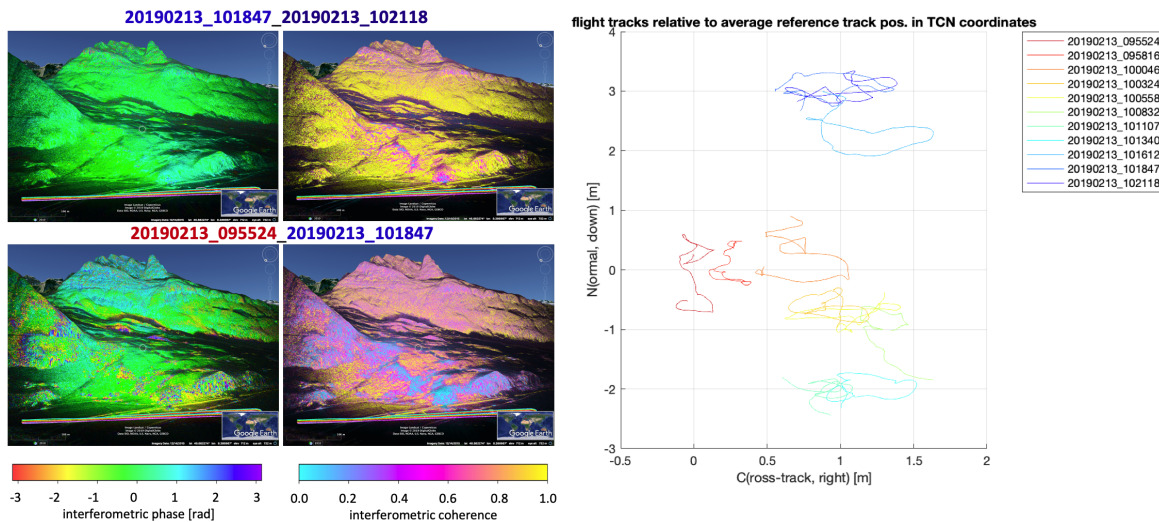
Fig. 4. UAV-borne repeat-pass DInSAR performance for different spatial baselines (plot on the right) in presence of vegetation/forested area: Interferometric phase $[-\pi, \pi]$ and coherence [0,1] for near-zero spatial baseline (top left) and for a baseline of approx. 3 m (bottom left).

and the high resolution provided by such car-borne or UAV-borne SAR system opens new and complementary possibilities to measure surface displacements of natural targets prone to temporal decorrelation and for measurements in adverse weather conditions.

REFERENCES

[1] H. Essen, W. Johannes, S. Stanko, R. Sommer, A. Wahlen, and J. Wilcke, "High resolution W-band UAV SAR," in *Proc. IEEE Int. Geosci. Remote Sens. Symp.*, July 2012, pp. 5033–5036.

[2] M. A. Remy, K. A. Camara de Macedo, and J. R. Moreira, "The first UAV-based P- and X-band interferometric SAR system," in *Proc. IEEE Int. Geosci. Remote Sens. Symp.*, July 2012, pp. 5041–5044.

[3] C. Stringham and D. G. Long, "GPU processing for UAS-based LFM-CW stripmap SAR," *Photogrammetric Engineering & Remote Sensing*, vol. 80, no. 12, pp. 1107–1115, 2014.

[4] O. Frey, C. L. Werner, U. Wegmuller, A. Wiesmann, D. Henke, and C. Magnard, "A car-borne SAR and InSAR experiment," in *Proc. IEEE Int. Geosci. Remote Sens. Symp.*, 2013, pp. 93–96.

[5] O. Frey, C. L. Werner, and U. Wegmuller, "GPU-based parallelized time-domain back-projection processing for agile SAR platforms," in *Proc. IEEE Int. Geosci. Remote Sens. Symp.*, July 2014, pp. 1132–1135.

[6] O. Frey, C. Magnard, M. Rüegg, and E. Meier, "Focusing of airborne synthetic aperture radar data from highly nonlinear flight tracks," *IEEE Trans. Geosci. Remote Sens.*, vol. 47, no. 6, pp. 1844–1858, June 2009.

[7] O. Frey, E. Meier, and D. Nüesch, "Processing SAR data of rugged terrain by time-domain back-projection," in *SPIE Vol. 5980: SAR Image Analysis, Modeling, and Techniques X*, 2005.

[8] M. Soumekh, *Synthetic Aperture Radar Signal Processing: with MATLAB Algorithms*. John Wiley & Sons, 1999.

[9] A. Ribalta, "Time-domain reconstruction algorithms for FMCW-SAR," *IEEE Geosci. Remote Sens. Lett.*, vol. 8, no. 3, pp. 396–400, May 2011.

[10] S. Palm, R. Sommer, A. Hommes, N. Pohl, and U. Stilla, "Mobile mapping by FMCW synthetic aperture radar operating at 300 GHZ," in *Int. Arch. Photogramm. Remote Sens. Spatial Inf. Sci., XLI-B1*, vol. XLI-B1. Copernicus GmbH, June 2016, pp. 81–87.

[11] S. Palm, R. Sommer, and U. Stilla, "Mobile radar mapping — subcentimeter SAR imaging of roads," *IEEE Transactions on Geoscience and Remote Sensing*, vol. 56, no. 11, pp. 6734–6746, Nov 2018.

[12] S. Stanko, W. Johannes, R. Sommer, A. Wahlen, J. Wilcke, H. Essen, A. Tessmann, and I. Kallfass, "SAR with MIRANDA - millimeterwave radar using analog and new digital approach," in *Proc. European Radar Conference*, Oct. 2011, pp. 214–217.

[13] M. Schuetz, M. Oesterlein, C. Birkenhauer, and M. Vossiek, "A custom lightweight UAV for radar remote sensing: Concept design, properties and possible applications," in *2017 IEEE MTT-S International Conference on Microwaves for Intelligent Mobility (ICMIM)*, March 2017, pp. 107–110.

[14] M. Lort, A. Aguasca, C. Lopez-Martinez, and T. M. Marin, "Initial evaluation of SAR capabilities in UAV multicopter platforms," *IEEE Journal of Selected Topics in Applied Earth Observations and Remote Sensing*, vol. 11, no. 1, pp. 127–140, Jan. 2018.

[15] D. Henke, M. Frioud, J. Fagir, S. Guillaume, M. Meindl, A. Geiger, S. Sieger, D. Janssen, F. Kloppel, M. Caris, S. Stanko, M. Renker, and P. Wellig, "Miranda35 experiments in preparation for small UAV-based SAR," in *Proc. IEEE Int. Geosci. Remote Sens. Symp.*, July 2019, pp. 8542–8545.

[16] M. Schartel, R. Burr, W. Mayer, and C. Waldschmidt, "Airborne tripwire detection using a synthetic aperture radar," *IEEE Geoscience and Remote Sensing Letters*, vol. 17, no. 2, pp. 262–266, Feb 2020.

[17] P. Hügler, T. Grebner, C. Knill, and C. Waldschmidt, "UAV-borne 2-D and 3-D radar-based grid mapping," *IEEE Geosci. Remote Sens. Lett.*, pp. 1–5, 2020.

[18] G. Ore, M. S. Alcantara, J. A. Goes, L. P. Oliveira, J. Yepes, B. Teruel, V. Castro, L. S. Bins, F. Castro, D. Luebeck, L. F. Moreira, L. H. Gabrielli, and H. E. Hernandez-Figueroa, "Crop growth monitoring with drone-borne DInSAR," *Remote Sensing*, vol. 12, no. 4, 2020.

[19] D. Luebeck, C. Wimmer, L. F. Moreira, M. Alcantara, O. Gian, J. A. Gós, L. P. Oliveira, B. Teruel, L. S. Bins, L. H. Gabrielli, and H. E. Hernandez-Figueroa, "Drone-borne differential SAR interferometry," *Remote Sensing*, vol. 12, no. 5, 2020.

[20] O. Frey, C. L. Werner, and R. Coscione, "Car-borne and UAV-borne mobile mapping of surface displacements with a compact repeat-pass interferometric SAR system at L-band," in *Proc. IEEE Int. Geosci. Remote Sens. Symp.*, 2019, pp. 274–277.

[21] E. Rodriguez and J. M. Martin, "Theory and design of interferometric synthetic aperture radars," *IEE Proceedings - Radar and Signal Processing*, vol. 139, no. 2, pp. 147–159, April 1992.

[22] P. Prats and J. J. Mallorqui, "Estimation of azimuth phase undulations with multisquint processing in airborne interferometric SAR images," *IEEE Trans. Geosci. Remote Sens.*, vol. 41, no. 6, pp. 1530–1533, 2003.